# High quality epitaxial $Mn_2Au$ (001) thin films grown by molecular beam epitaxy

S.P. Bommanaboyena[1], T. Bergfeldt[2], R. Heller[3], M. Kläui[1] and M. Jourdan[1]
[1]Institute of Physics, Johannes Gutenberg-University, 55099 Mainz, Germany
[2]Institute for Applied Materials-Applied Materials Physics, Karlsruhe Institute of Technology, 76344 Eggenstein-Leopoldshafen, Germany
[3]Institute of Ion Beam Physics and Materials Research, Helmholtz-Zentrum Dresden-Rossendorf, 01328 Dresden, Germany

## Abstract

The recently discovered phenomenon of Néel spin-orbit torque in antiferromagnetic $Mn_2Au$ [1, 2, 3] has generated huge interest in this material for spintronics applications. In this paper, we report the preparation and characterization of high quality $Mn_2Au$ thin films by molecular beam epitaxy and compare them with magnetron sputtered samples. The films were characterized for their structural and morphological properties using reflective high-energy electron diffraction, X-ray diffraction, X-ray reflectometry, atomic force microscopy and temperature dependent resistance measurements. The thin film composition was determined using both inductively coupled plasma optical emission spectroscopy and Rutherford backscattering spectrometry techniques. The MBE grown films were found to show a superior smooth morphology and a low defect concentration resulting in reduced scattering of the charge carriers.

## Introduction

Though ferromagnetic materials (FMs) have dominated the field of spintronics since its inception, the last few years witnessed a rather sudden interest in antiferromagnetic materials (AFMs) for spintronics applications. Attractive features such as insensitivity to strong external magnetic fields, lack of stray fields and ultrafast magnetization dynamics have gradually paved the way to an emerging realm of 'antiferromagnetic spintronics' and provide strong motivation for the investigation of AFMs on par with FMs for next generation electronics. The recent prediction [4] and experimental realization of Néel order switching in antiferromagnets with specific crystallographic symmetry using current induced staggered spin-orbit fields [1, 2, 3, 5] is a true testimony to the hitherto untapped potential held by AFMs. This aptly named Néel spin-orbit torque (NSOT) is capable of switching the Néel vector between two stable configurations in centrosymmetric AFMs where the two magnetic sublattices form inversion partners while having a locally broken structure inversion symmetry (Figure 1). Presently, CuMnAs and $Mn_2Au$ are the only two AFMs known to possess the requisite symmetry. Subsequently, the reoriented antiferromagnetic order parameter can be monitored by measuring the corresponding change in resistance (anisotropic magnetoresistance or AMR effect) of the structure. Reversible switching between the two stable states using extremely short current pulses enables these AFMs to be used for information storage as demonstrated recently in a fully integrated memory device [6].

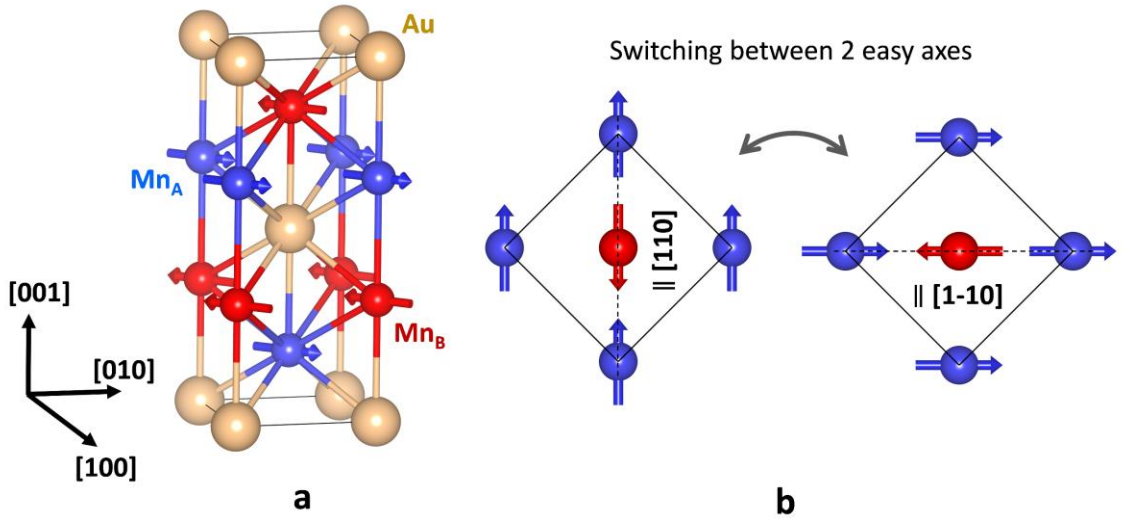


Figure 1.a. Unit cell of $Mn_2Au$. It is seen to be centrosymmetric with the two magnetic sublattices A and B forming spatial inversion partners with respect to the central Au atom which serves as an inversion centre. The inversion symmetry is locally broken on individual magnetic sublattices along [001]. b. The two orthogonal easy axes of $Mn_2Au$ (represented by dotted lines). The magnetic moments can be reversibly switched between these two states via NSOT.

$Mn_2Au$ is considered to be a favourable option due to its large spin-flop transition field, high Néel temperature [7] and lack of toxic elements. Up to now, all available $Mn_2Au$ thin films were grown by MBE in (101)-orientation [8], or by sputtering in (001)-orientation [2, 9, 10], as well as in (110)- [10] (103)-, (101)-, and (204)-orientation [11]. However, (001)-axis grown films are favourable to observe NSOT switching as in this case the quasi-easy plane is parallel to the substrate plane. (001)-oriented $Mn_2Au$ thin films were first grown by Jourdan et al. via RF magnetron sputtering from a stoichiometric target onto an epitaxial Ta (001) buffer layer deposited on r-plane $Al_2O_3$ substrate [9]. The films were found to be quasi-epitaxial with a relatively rough morphology. Meinert et al. reported epitaxial $Mn_2Au$ thin films grown by DC magnetron co-sputtering of Au and Mn onto epitaxial ZrN (001) buffer layer deposited on MgO (001) substrate [2]. They found a trade-off between morphology and crystallinity. Here we show that it is possible to overcome these problems by improving upon our previous growth technique [9]. Smooth surface features are important to observe NSOT induced antiferromagnetic domain wall motion and good crystal quality is required to study the band structure of materials using photoemission. We deposited $Mn_2Au$ thin films using molecular beam epitaxy and magnetron sputtering and incorporated a post-deposition annealing step into the fabrication procedure in both cases. The films were subjected to various characterization procedures to understand their crystallographic phase, topography and composition. The preparation and characterization details are presented in the following sections.

## Thin film growth parameters

10 x 10 x 0.53 mm, single side polished r-plane $Al_2O_3$ substrates from CrysTec GmbH were used for these experiments. The substrates were annealed in UHV at 550°C for 30 minutes prior to deposition to get rid of adsorbed water and organic contamination. $Mn_2Au$ has a tetragonal structure with a = 3.32 Å and c = 8.53 Å. Body centred cubic Ta has a lattice constant of 3.30 Å and therefore serves as an ideal buffer layer for $Mn_2Au$ (001) due to the small lattice mismatch of 0.6%. First, a 13 nm thick epitaxial Ta (001) buffer layer was deposited on $Al_2O_3$ at 450°C via RF magnetron sputtering. The sample was then transferred to the MBE chamber under UHV conditions. Subsequently, a 45 nm $Mn_2Au$ film was grown over the Ta buffer

by co-evaporation of high purity Mn and Au from separate sources in high vacuum. The base pressure of our MBE chamber is 7 x $10^{-10}$ mbar while the working pressure is 1 x $10^{-7}$ mbar. Mn was evaporated from a high temperature effusion cell with a stable evaporation rate which was predetermined by XRR analysis of a pure Mn film. An electron beam evaporator was used to evaporate Au and its rate was continuously monitored during deposition using an oscillating quartz crystal monitor. Mn and Au were simultaneously deposited on the Ta buffer at a rate of 0.23 Å/sec and 0.15 Å/sec respectively corresponding to a ratio of 1.5:1 which results in stoichiometric $Mn_2Au$ as we will explain below. The substrate temperature was maintained at 270°C during deposition. Subsequently, the films were annealed at 450°C for 60 minutes. Both temperature and duration of this post-deposition annealing step were found to be crucial for the formation of a smooth and well-ordered crystal. Additionally, a sample with the same thickness was prepared by RF magnetron sputtering from a stoichiometric $Mn_2Au$ target for comparison. The base pressure of our sputtering chamber is 1.5 x $10^{-8}$ mbar. 45 nm $Mn_2Au$ was sputtered onto r-plane $Al_2O_3$ / 13 nm Ta (001) at 300°C and 0.1 mbar Ar pressure with a deposition rate of 0.75 Å/sec. The Ta buffer layer was grown in the same way as explained above. The films were subjected to the same post-deposition annealing step as the MBE samples.

## Crystallographic and morphological characterization

In-situ reflective high-energy electron diffraction (RHEED) was performed after cooling the samples to room temperature to check both crystal quality and surface features. Sharp diffraction spots on semi-circles are observed in both cases (Figure 2), indicating a highly crystalline and smooth surface. Both samples also reveal the presence of Kikuchi lines, implying a low concentration of crystallographic defects at the surface compared to our previously reported $Mn_2Au$ films [9]. This was further verified using X-ray reflectometry (XRR) measurements as shown in Figure 6.

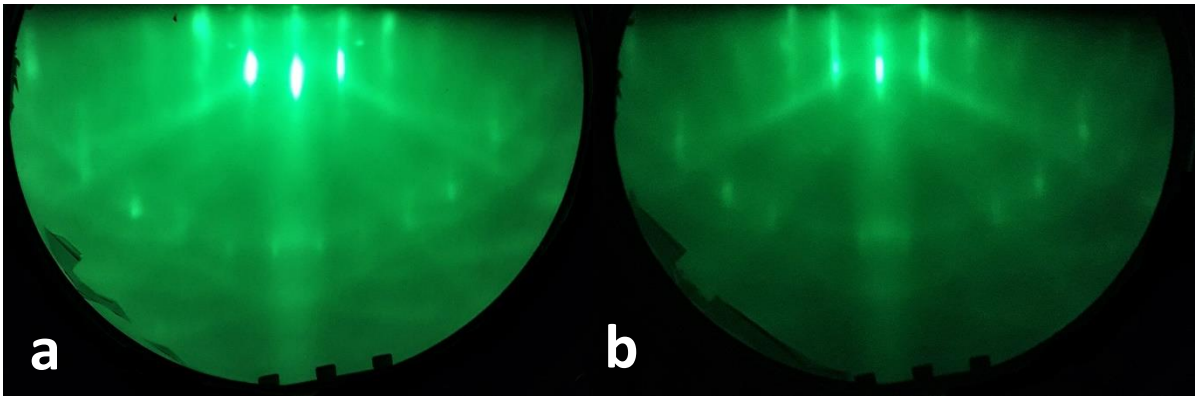


Figure 2.a. RHEED pattern of $Al_2O_3$ (1-102) / 13 nm Ta (001) / 45 nm $Mn_2Au$ (001). a. MBE sample. b. Sputtered sample. The arrangement of the spots on semicircles and the Kikuchi lines indicate a smooth morphology with a low defect concentration at the surface.

The X-ray diffraction (XRD) specular Θ/2Θ scans shown in Figure 3 reveal the presence of (001)-oriented $Mn_2Au$ in both samples. The sputtered sample additionally shows a very small fraction of (101)-orientation. Compared to our previous samples [9], this undesired orientation has been largely eliminated by optimizing the deposition temperature and by adding the post-deposition annealing procedure. Both

samples have a mosaicity of 0.5° as can be inferred from the width of the rocking curve of the (002) peak (ω-scan) shown in the inset.

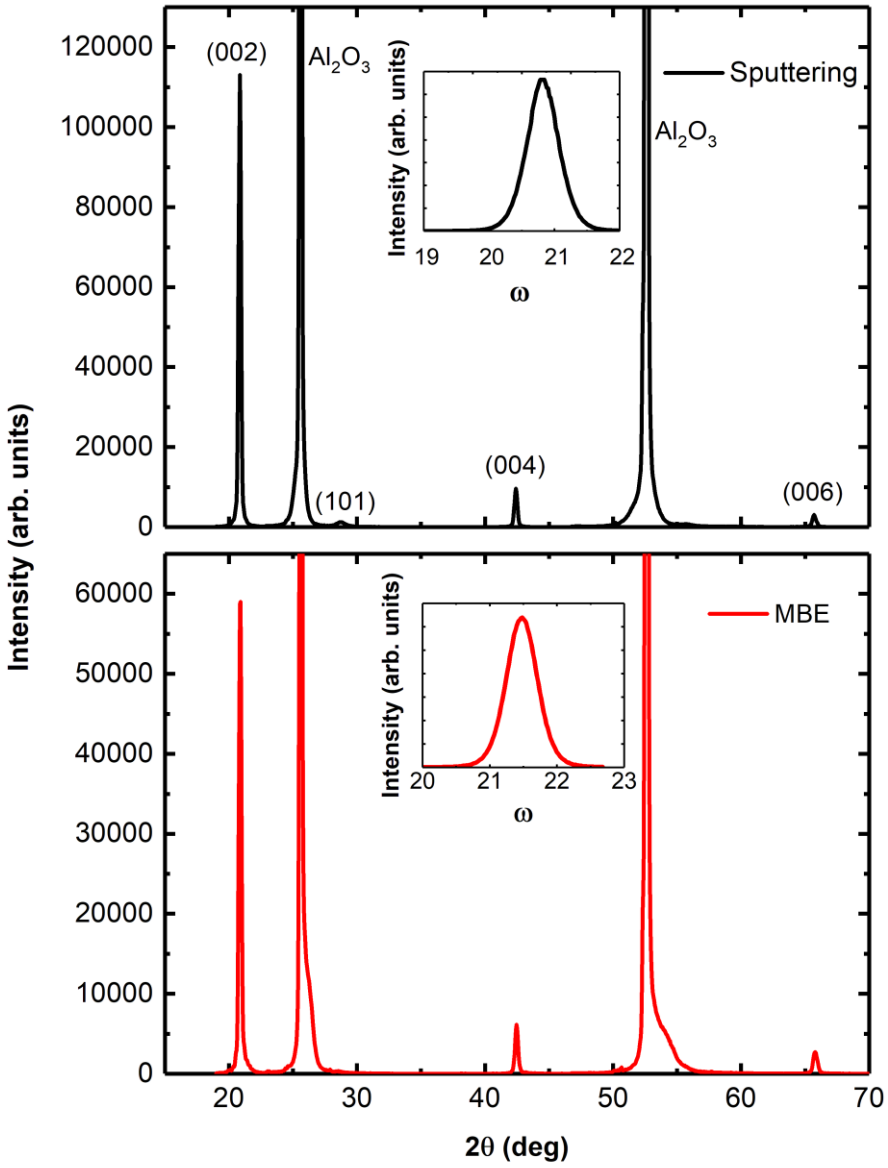


Figure 3. Θ/2Θ XRD specular scans of $Al_2O_3$ (1-102) / 13 nm Ta (001) / 45 nm $Mn_2Au$ (001) demonstrating the (001)-orientation of the sputtered (upper panel) as well as of the MBE grown (lower panel) samples. A very small fraction of (101)-orientation is visible for sputtered samples which does not appear in the case of MBE grown thin films. The rocking curves of the (002) $Mn_2Au$ peak shown in the insets reveal a mosaicity of 0.5° for both types of samples. The (002) peak of Ta occurs at 55° but has a very low intensity due to the small thickness of this layer. Therefore, it is not visible on this scale.

Figure 4 shows the in-plane order of $Mn_2Au$ with the help of off specular XRD ϕ-scans of $Mn_2Au$ (101) and Ta (220) peaks. $Mn_2Au$ [100] is oriented parallel to Ta [100] as expected based on the lattice match. The

same type of investigation of sputtered samples results in very similar data, leading to the conclusion that the degree of in-plane crystallographic ordering of both MBE-grown and sputtered samples is very high.

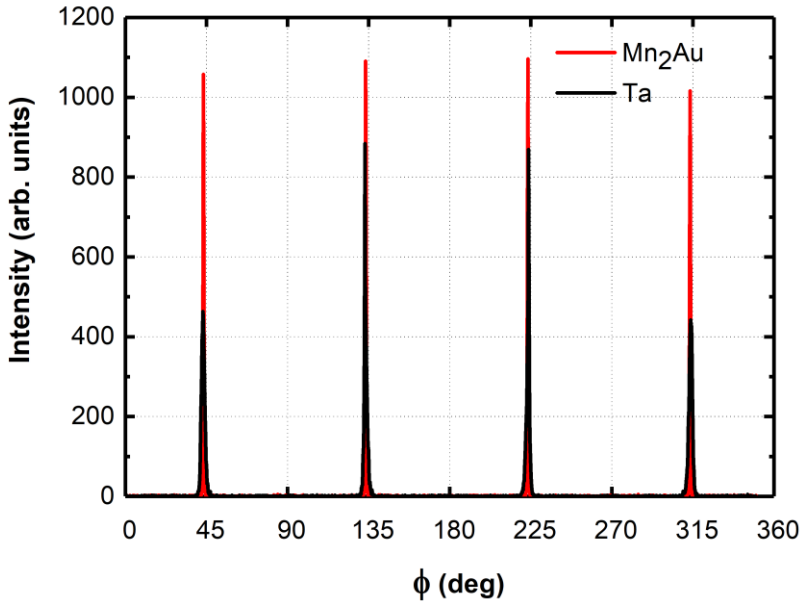


Figure 4. XRD ϕ-scans of off-specular $Mn_2Au$ (101) and Ta (220) peaks of $Al_2O_3$ (1-102) / 13 nm Ta (001) / 45 nm $Mn_2Au$ (001) MBE sample. The scans confirm the 4-fold symmetry of the $Mn_2Au$ crystal and shows a very high degree of in-plane order with $Mn_2Au$ [100] ∥ Ta [100] alignment.

The MBE co-deposition of Mn and Au from separate sources with independent rate control offers the opportunity of controlled variation of the sample composition. However, at the same time it is challenging to obtain a stoichiometric composition of the $Mn_2Au$ thin films. Furthermore, the analysis of the composition of thin films requires special methods, as many of the standard techniques for bulk samples such as x-ray fluorescence (XRF) and energy dispersive x-ray spectroscopy (EDX) in general deliver unreliable results for thin films. However, after a careful adjustment of the deposition rates, we were able to obtain MBE grown $Mn_2Au$ thin films with a stoichiometric composition (66.6 ± 1.2 at% Mn and 33.4 ± 1.7 at% Au) as determined by inductively coupled plasma optical emission spectroscopy (ICP-OES). The sputtered samples were found to have a composition of 66.1 ± 1.2 at% Mn and 33.9 ± 1.7 at% Au. This was further verified using Rutherford backscattering spectrometry (RBS) which found the stoichiometry values to be within the error margin mentioned above. Interestingly, both analysis techniques revealed that for annealing temperatures higher than 450°C, Mn begins to desorb from the film changing both its stoichiometry and crystallographic phase. For instance, a sample annealed at 500°C was found to be polycrystalline and comprising of 56.6% Mn and 43.3% Au. Additionally, RBS revealed that this sample contained an 8 nm thick Mn-Au-Ta alloy layer between the buffer and $Mn_2Au$ layers due to thermally activated diffusion of Ta atoms into the overlying film.

Although X-ray diffraction probes the crystallographic order of the samples, its sensitivity for low degrees of disorder, which nevertheless influences the transport properties, is limited. A figure of merit for the concentration of impurities, which results in scattering of the charge carriers in metals, is the residual resistance ratio (RRR) = $Resistance_{300K}$ / $Resistance_{4K}$. Thus, we performed temperature dependent sheet

resistivity measurements of both MBE deposited and sputtered $Mn_2Au$ films grown under optimized conditions (Figure 5) using the van der Pauw method. Though the resistivity of both films is the same at 300K, the MBE film has a lower resistivity at 4K (a temperature where phonon scattering is suppressed) implying a lower level of intrinsic disorder. The MBE film shows RRR $\simeq$ 6.8 while the value for the sputtered film is RRR $\simeq$ 4.6. These values represent a significant improvement in quality over that of the previously reported films, which showed a residual resistivity of 7 μΩ.cm and RRR $\simeq$ 3 [9].

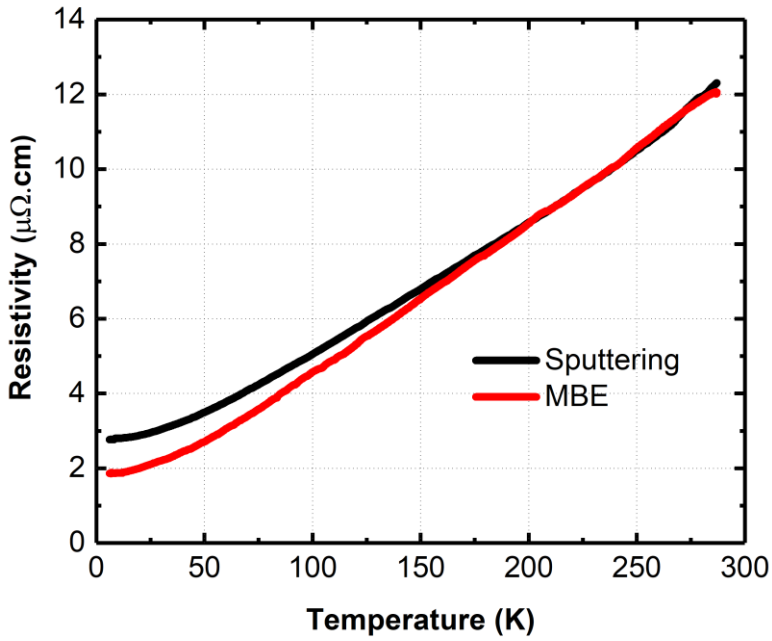


Figure 5. Resistivity vs. temperature measurements of 45 nm $Mn_2Au$ (001) films. The buffer layer contribution was eliminated by measuring resistance vs. temperature of a $Al_2O_3$ (1-102) / 13 nm Ta (001) sample and subtracting it from the resistance of $Al_2O_3$ (1-102) / 13 nm Ta (001) / 45 nm $Mn_2Au$ (001) using a parallel resistance model. Compared to the sputtered sample reduced residual resistivity of the MBE thin film indicates a lower degree of disorder achieved by MBE deposition.

Furthermore, superior smoothness of our MBE grown samples is evident from the presence of prominent Kiessig fringes corresponding to the 45 nm $Mn_2Au$ layer in its XRR scan in Figure 6. The sputtered sample mainly shows oscillations corresponding to the 13 nm Ta buffer layer. Though faint fringes corresponding to the $Mn_2Au$ layer are also present at lower angles, they fade away rather quickly with increasing angle due to its relatively poor morphology.

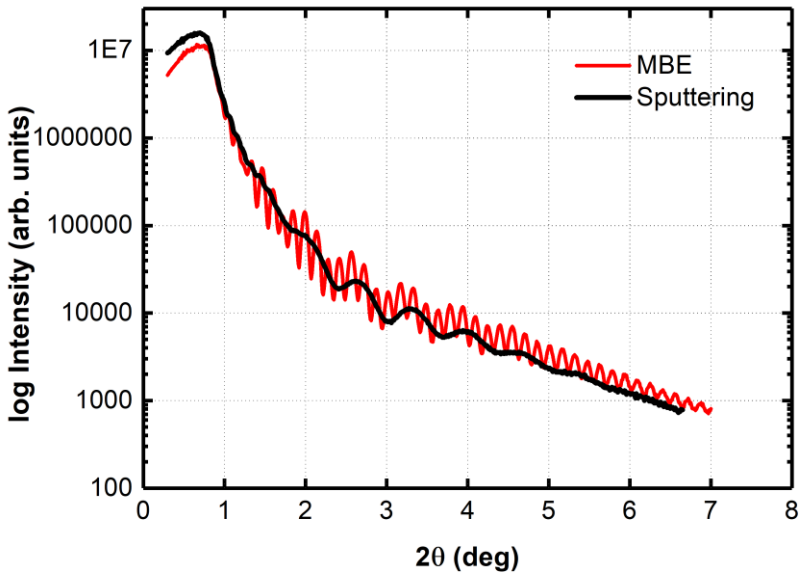


Figure 6. Comparison of the XRR scans of $Al_2O_3$ (1-102) / 13 nm Ta (001) / 45 nm $Mn_2Au$ (001) films grown via MBE and sputtering techniques. The sputtered sample shows very weak oscillations corresponding to the thickness of the $Mn_2Au$ layer at lower angles, whereas prominent oscillations are observed in case of the MBE sample even at higher angles. This is due to smoother morphology of the MBE sample compared to the sputtered sample.

More direct information about the morphology of our films was also obtained by atomic force microscopy and the results are shown in Figure 7. The MBE film has a more homogeneous topography compared to the sputtered sample, which is consistent with the XRR results discussed above.

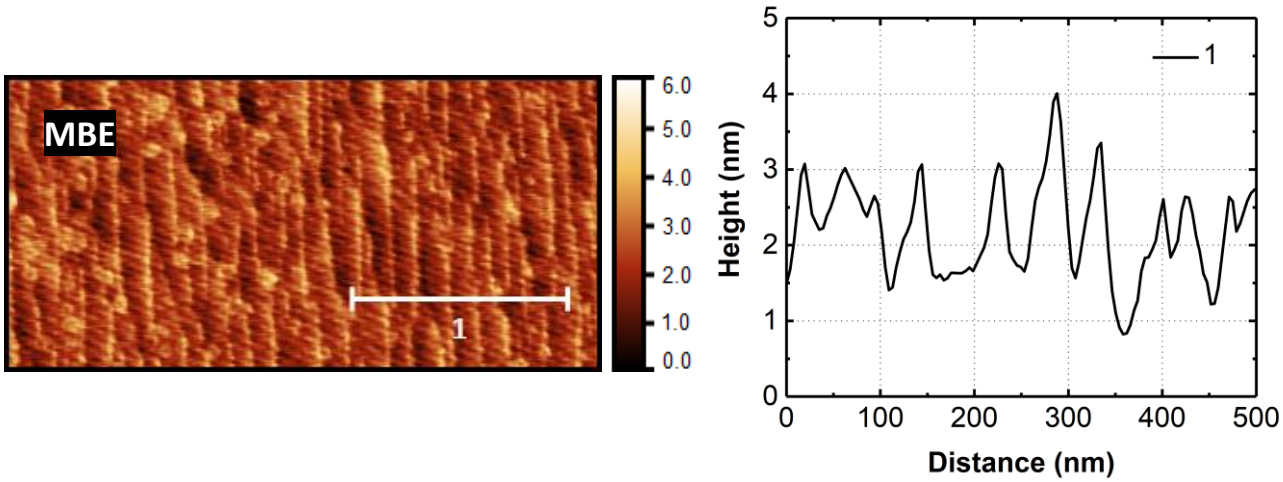


Figure 7.a. Atomic force microscopy scan of MBE grown $Al_2O_3$ (1-102) / 13 nm Ta (001) / 45 nm $Mn_2Au$ (001) film. The regular ripple structure slightly tilted with respect to the horizontal is an artefact of the

measurement. The plot on the right side depicts a height profile along the horizontal marked in the topography image.

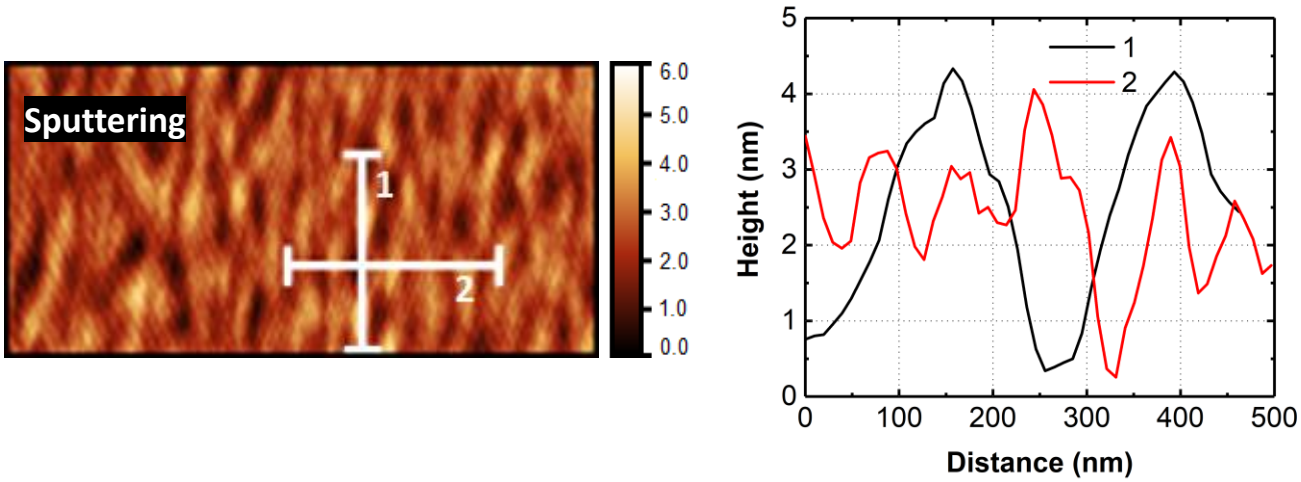


Figure 7.b. Atomic force microscopy scan of a sputtered $Al_2O_3$ (1-102) / 13 nm Ta (001) / 45 nm $Mn_2Au$ (001) film. The plot on the right side depicts height profiles along the lines marked in the topography image.

Whereas the typical peak to valley difference in the MBE grown samples amounts to ≈1-2 nm, it is about 4 times larger in sputtered samples. This is expected to result in larger AFM domains in the MBE samples as well as in reduced domain wall pinning. However, this will require further investigations similar to our previous work on the sputtered samples [3, 12].

## Conclusion

We demonstrated a substantially improved crystallinity and morphology of $Mn_2Au$ (001) thin films for antiferromagnetic spintronics due to optimized growth conditions and using MBE as an alternative deposition technique. By adding an annealing procedure after the sample deposition both morphology and epitaxial quality were improved. Furthermore, by using MBE instead of sputtering, the degree of disorder in the thin films which is relevant for electrical transport was clearly reduced. Most importantly, the MBE grown thin films show a significantly smoother morphology. This is promising for future spintronics devices, which potentially require reduced domain wall pinning, larger AFM domains and often rely on well-defined smooth interfaces of different functional layers.

## Acknowledgments

Funded by the Deutsche Forschungsgemeinschaft (DFG, German Research Foundation) – TRR 173 – 268565370 (project A05 and B12). Financial support by the European Commission FET Open RIA ASPIN (Project no. 766566) is acknowledged. S.P.B acknowledges financial support from the Max Planck Graduate Center.

## Data Availability Statement

The data that supports the findings of this study are available within the article [and its supplementary material].

## References


[1] S. Yu. Bodnar, L. Šmejkal, I. Turek, T. Jungwirth, O. Gomonay, J. Sinova, A. A. Sapozhnik, H.-J. Elmers, M. Kläui & M. Jourdan, *Nat. Commun.*, **9**, 348 (2018).

[2] M. Meinert, D. Graulich & T. Matalla-Wagner, *Phys. Rev. Appl.*, **9**, 064040 (2018).

[3] S. Yu. Bodnar, M. Filianina, S. P. Bommanaboyena, T. Forrest, F. Maccherozzi, A. A. Sapozhnik, Y. Skourski, M. Kläui, & M. Jourdan, *Phys. Rev. B*, **99**, 140409(R) (2019).

[4] J. Železný, H. Gao, K. Výborný, J. Zemen, J. Mašek, A. Manchon, J. Wunderlich, J. Sinova & T. Jungwirth, *Phys. Rev. Lett.*, **113**, 157201 (2014).

[5] P. Wadley, B. Howells, J. Železný, C. Andrews, V. Hills, R. P. Campion, V. Novák, K. Olejník, F. Maccherozzi, S. S. Dhesi, S. Y. Martin, T. Wagner, J. Wunderlich, F. Freimuth, Y. Mokrousov, J. Kuneš, J. S. Chauhan, M. J. Grzybowski, A. W. Rushforth, K. W. Edmonds, B. L. Gallagher, T. Jungwirth, *Science*, **351**, 587 (2016).

[6] K. Olejník, V. Schuler, X. Marti, V. Novák, Z. Kašpar, P. Wadley, R. P. Campion, K. W. Edmonds, B. L. Gallagher, J. Garces, M. Baumgartner, P. Gambardella & T. Jungwirth, *Nat. Commun.*, **8**, 15434 (2017).

[7] V. M. T. S. Barthem, C. V. Colin, H. Mayaffre, M. H. Julien & D. Givord, *Nat. Commun.*, **4**, 2892 (2013).

[8] H.-C. Wu, Z.-M. Liao, R. G. S. Sofin, G. Feng, X.-M. Ma, A. B. Shick, O. N. Mryasov & I. V. Shvets, *Adv. Mat.*, **24**, 6374 (2012).

[9] M. Jourdan, H. Bräuning, A. Sapozhnik, H.-J. Elmers, H. Zabel & M. Kläui, *J. Phys. D : Appl. Phys.*, **48**, 385001 (2015).

[10] M. Arana, F. Estrada, D. S. Maior, J. B. S. Mendes, L. E. Fernandez-Outon, W. A. A. Macedo, V. M. T. S. Barthem, D. Givord, A. Azevedo, & S. M. Rezende, *Appl. Phys. Lett.*, **111**, 192409 (2017).

[11] X. F. Zhou, J. Zhang, F. Li, X. Z. Chen, G. Y. Shi, Y. Z. Tan, Y. D. Gu, M. S. Saleem, H. Q. Wu, F. Pan, & C. Song, *Phys. Rev. Appl.*, **9**, 054028 (2018)

[12] A. A. Sapozhnik, M. Filianina, S. Yu. Bodnar, A. Lamirand, M.-A. Mawass, Y. Skourski, H.-J. Elmers, H. Zabel, M. Kläui, & M. Jourdan, *Phys. Rev. B*, **97,** 134429 (2018).